Redox regulation by TXNRD3 during epididymal maturation underlies capacitation-associated mitochondrial activation and sperm motility in mice

Huafeng Wang[1], Qianhui Dou[2], Kyung Jo Jung[3], Jungmin Choi[3,4], Vadim N. Gladyshev[2], Jean-Ju Chung[1,5*]

[1]Departmet of Cellular and Molecular Physiology, Yale School of Medicine, New Haven, CT, United States

[2]Division of Genetics, Department of Medicine, Brigham and Women's Hospital, Harvard Medical School, Boston, MA, United States

[3]Department of Biomedical Sciences, Korea University College of Medicine, Seoul, South Korea

[4]Department of Genetics, Yale School of Medicine, Yale University, New Haven, CT, United States

[5]Department of Obstetrics, Gynecology, and Reproductive Sciences, Yale School of Medicine, New Haven, CT, United States

*** Correspondence:** Jean-Ju Chung (jean-ju.chung@yale.edu)

Keywords: Thioredoxin Glutathione Reductase, TXNRD3, Redox homeostasis, male fertility, mitochondrial function, Ultrastructure.

Abstract

During epididymal transit, redox remodeling protects mammalian spermatozoa, preparing them for survival in the subsequent journey to fertilization. However, molecular mechanisms of the redox regulation in sperm development and maturation remain largely elusive. In this study, we report thioredoxin reductase 3 (TXNRD3) - a thioredoxin reductase family member particularly abundant in elongating spermatids at the site of mitochondrial sheath formation - contributes to regulate redox homeostasis in male reproduction. Using *Txnrd3*$^{-/-}$ mice, our biochemical, ultrastructural, and live cell imaging analyses revealed impairments in sperm morphology and motility in absence of TXNRD3. Absence of TXNRD3 alters redox status in both the head and tail during sperm maturation and capacitation, resulting in defective mitochondrial ultrastructure and activity under capacitating conditions. These findings provide insights into molecular mechanisms of redox homeostasis and bioenergetics during sperm maturation, capacitation, and fertilization.

Introduction

Testicular sperm are functionally immature in that they lack the ability to naturally fertilize an egg. Epididymis transit is an indispensable step for mammalian sperm cells to fully develop fertilizing ability. During epididymal descent, spermatozoa acquire the potential to develop progressive motility and capacitation (Sullivan and Mieusset 2016, Gervasi and Visconti 2017). One major threat to sperm for the subsequent journey to fertilization is their extreme susceptibility to oxidative damage since their plasma membrane is rich in polyunsaturated fatty acids (Vernet, Aitken et al. 2004). Redox mechanisms prepare epididymal spermatozoa for their protection and survival during the fertilization journey (Chabory, Damon et al. 2009). For example, reactive oxygen species (ROS) generation is a physiological event required for mammalian sperm maturation, capacitation, acrosome reaction. At the same time, increase of oxidative damage correlates with lower motility in human sperm (Kao, Chao et al. 2008) and causes DNA fragmentation and protein crosslinking (Henkel, Kierspel et al. 2005). However, it remains unclear how redox homeostasis is maintained during mammalian sperm capacitation.

To date, thioredoxin and glutathione systems are two major redox systems responsible for coping with oxidative stress distinctly and divergently. Thioredoxin reductases, a family of selenium-containing pyridine nucleotide-disulfide oxidoreductases, are key redox regulators of mammalian thioredoxin system. They are comprised of three isoenzymes: thioredoxin reductase 1 (TXNRD1), thioredoxin reductase 2 (TXNRD 2) and thioredoxin-glutathione reductase (TXNRD3, also known as TGR)(Holmgren 1980, Mustacich and Powis 2000). Cytosolic TXNRD1 and mitochondrial TXNRD2 are implicated in redox regulation during cell growth and embryogenesis (Arnér and Holmgren 2000, Conrad, Jakupoglu et al. 2004, Nalvarte, Damdimopoulos et al. 2004, Jakupoglu, Przemeck et al. 2005). TXNRD3 is predominantly expressed in testis (Sun, Kirnarsky et al. 2001) and particularly abundant in elongating spermatids at the site of mitochondrial sheath formation (Su, Novoselov et al. 2005). Structurally, TXNRD3 uniquely contains an additional N-terminal glutaredoxin domain compared with the other two TXNRD isozymes (Sun, Kirnarsky et al. 2001). Disulfide bond isomerase activity of TXNRD3 was previously reported *in vitro* (Su, Novoselov et al. 2005), yet the physiological significance and underlying mechanisms of TXNRD3 in male germ cell development and sperm function have been largely unknown. In the accompanying study, we

report that *Txnrd3*$^{-/-}$ mice exhibit compromised male fertility, with mild impregnation delay *in vivo* and diminished sperm fertilization capacity *in vitro* (Dou et al., 2021).

Here, we report the underlying mechanism of TXNRD3 function in regulation of chromatin organization and mitochondrial activity during sperm capacitation in mice. We find that targeted disruption of *Txnrd3* induces capacitation-associated impairment in sperm morphology and motility. Biochemical analyses demonstrate that TXNRD3 expression diminishes during sperm maturation, impairing redox homeostasis of head and flagellar proteins. Using ultrastructural analyses and live cell imaging, we reveal that mitochondria in *Txnrd3*$^{-/-}$ sperm undergo structural defects and lose control of its activity especially during sperm capacitation. These findings provide insights into sperm redox regulation during epididymal maturation and its effect on capacitation-associated energy metabolism.

Materials and methods

Mouse Sperm Preparation and *in vitro* Capacitation

Epididymal spermatozoa from adult male mice were collected by swim-out from caudal epididymis in standard HEPES saline (HS) medium (in mM, 135 NaCl, 5 KCl, 1 $MgSO_4$, 2 $CaCl_2$, 20 HEPES, 5 Glucose, 10 Lactic acid, 1 Na pyruvate, pH 7.4 adjusted with NaOH, 320 mOsm/L). 2×10^6 cells/ml sperm were incubated in human tubular fluid (HTF) medium (EMD Millipore) at 37°C, 5% CO_2 for 90 min to induce capacitation.

Antibodies and Reagents

Rabbit polyclonal antibodies specific to mouse TXNRD3 and GPX4 (Su, Novoselov et al. 2005) were described previously. All the other antibodies used in this study are commercially available as follows (ANT4, Abcam; P2X2, Santa Cruz; TOM20, Santa Cruz; TXNRD1, Bioss Antibodies; TXNRD2, Proteintech; acetylated tubulin, Sigma). All the chemicals were from Sigma Aldrich unless otherwise indicated.

Single-cell RNA-seq analysis

The raw count matrices for human (GSE109037) and mouse (GSE109033) testis single cell RNA (scRNA)-seq datasets (Hermann, Cheng et al. 2018) were downloaded from Gene Expression Omnibus (GEO) database (https://www.ncbi.nlm.nih.gov/geo/). The downloaded raw count matrices were processed for quality control using the Seurat package (ver.3.2.3) (Stuart, Butler et al. 2019). Briefly, cells with less than 200 expressed features, higher than 9,000 (GSE109033) or

10,000 (GSE109037) expressed features and higher than 20% (GSE109037) or 25% (GSE109033) mitochondrial transcript fraction were excluded to select single-cells with high quality mRNA profiles. The data was normalized by the total expression, scaled and log transformed. Identification of 2,000 highly variable features was followed by PCA to reduce the number of dimensions representing each cell. Statistically significant 15 PCs were selected based on the JackStraw and Elbow plots and provided as input for constructing a K-nearest-neighbors (KNN) graph based on the Euclidean distance in PCA space. Cells were clustered by the Louvain algorithm with a resolution parameter 0.1. Uniform Manifold Approximation and Projection (UMAP) was used to visualize and explore cluster data. Marker genes that define each cluster were identified by comparing each cluster to all other clusters using the MAST (Finak, McDavid et al. 2015) provided in Seurat package. In order to correct batch effects among samples and experiments, we applied the Harmony package (ver.1.0) (Korsunsky, Millard et al. 2019) to the datasets. The Markov Affinity-based Graph Imputation of Cells (MAGIC) algorithm (ver.2.0.3) (van Dijk, Sharma et al. 2018) was used to denoise and the count matrix and impute the missing data. In these testis datasets from adult human, we identified 23,896 high quality single cells, that were clustered into 7 major cell types, including spermatogonia, spermatocytes, early spermatids, late spermatids, peritubular myoid cell, endothelial cell, and macrophage. Similarly, we exploited 30,268 high quality single cells from eight adult and three 6-day postpartum mouse testis tissue samples and subsequently defined 11 major cell populations.

Sperm Immunocytochemistry and Free thiol Labeling Assay

Mouse and human sperm were washed in PBS twice, attached on the glass coverslips, and fixed with 4% paraformaldehyde (PFA) in PBS at room temperature (RT) for 10 minutes (mouse) or at 4°C for 1 hr (human). Fixed samples were permeabilized using 0.1% Triton X-100 in PBS at RT for 10 minutes, washed in PBS, and blocked with 10% goat serum in PBS at RT for 1 hr. Cells were stained with antibody in PBS supplemented with 10% goat serum at 4°C overnight. After washing in PBS, the samples were incubated with goat anti-rabbit Alexa 647 or Alexa 555-plus (Invitrogen, 1:1,000) in 10% goat serum in PBS at RT for 1 hr. Hoechst was used to counterstain nucleus for sperm head. For BODIPY-N-ethylmaleimide labeling, reduced thiols within proteins were alkylated with BODIPY FL maleimide (final concentration of 10 nM, ThermoFisher) for 30 min in the dark after permeabilization. The sample was then quenched by addition of 500 mM 2-mercaptoethanol for 30 min in the dark, followed by 3 times washing in PBS. For ThiolTracker

122 (ThermoFisher) labeling, fixed sperm were stained with 20 μM dye, followed by 3 times washing
123 in PBS. Stained sperm samples were mounted with Prolong gold (Invitrogen) and cured for 24 hr,
124 followed by imaging with Zeiss LSM710 Elyra P1 using Plan-Apochrombat 63X/1.40 or alpha
125 Plan-APO 100X/1.46 oil objective lens (Carl Zeiss).

126 **Protein Extraction and Western Blotting**

127 Whole sperm protein was extracted as previously described(Chung, Navarro et al. 2011, Chung,
128 Shim et al. 2014, Chung, Miki et al. 2017). In short, mouse epididymal spermatozoa washed in
129 PBS were directly lysed in 2× SDS sample buffer or 8 M urea. The whole sperm lysate was
130 centrifuged at 15,000 g, 4°C for 10 min. Supernatant were adjusted to 50 mM DTT and denatured
131 at 95°C for 10 min before loading to gel. The membranes were incubated overnight at 4°C with
132 primary antibody, followed by washing with PBST and incubation with appropriate secondary
133 antibody for 1 hr. Bands were visualized using chemiluminescence and imaged by ChemiDoc
134 (Bio-Rad). Antibodies used for Western blotting were rabbit anti-mouse TXNRD3 (1:2000), GPx4
135 (1:2000), ANT4, 1 μg/mL; P2X2, 1 μg/mL; TOM20, 0.2 μg/mL; TXNRD1, 1 μg/mL; TXNRD2,
136 1 μg/mL; acetylated tubulin and anti-acetylated tubulin (1: 20,000). Secondary antibodies were anti-
137 rabbit IgG-HRP (1:10,000) and anti-mouse IgG-HRP (1:10,000) from Jackson ImmunoResearch
138 (West Grove, PA).

139 **Protein oxidation**

140 Carbonyl groups inserted into proteins by oxidative reactions were evaluated with protein carbonyl
141 assay kit (Abcam). Briefly, samples were homogenized and processed according to the
142 manufacturer's protocol. The carbonyl groups in the solubilized protein samples were derivatized
143 using DNPH (2, 4 dinitrophenyl hydrazine) or control solution for 15 min and then neutralized.
144 The samples were then loaded onto SDS PAGE gels and DNP conjugated proteins were detected
145 by western blotting using primary DNP antibody and HRP conjugated secondary antibody.

146 **Flagella Waveform Analysis**

147 To tether sperm head for planar beating, non-capacitated or capacitated spermatozoa (2-3×10^5 cells)
148 from adult male mice were transferred to the fibronectin-coated 37°C chamber for Delta T culture
149 dish controller (Bioptechs) filled with HS and HEPES-buffered HTF medium (H-HTF)(Chung,
150 Miki et al. 2017), respectively. Flagellar movements of the tethered sperm were recorded for 2 s
151 with 200 fps using pco.edge sCMOS camera equipped in Axio observer Z1 microscope (Carl
152 Zeiss). All movies were taken at 37°C within 10 minutes after transferring sperm to the imaging

153 dish. FIJI software (Schindelin, Arganda-Carreras et al. 2012) was used to measure beating
154 frequency of sperm tail, and to generate overlaid images to trace waveform of sperm flagella as
155 previously described (Chung, Miki et al. 2017).

156 **Sperm motility analysis**

157 Aliquots of sperm were placed in slide chamber (CellVision, 20 mm depth) and motility was
158 examined on a 37°C stage of a Nikon E200 microscope under 10X phase contrast objective (CFI
159 Plan Achro 10X/0.25 Ph1 BM, Nikon). Images were recorded (40 frames at 50 fps) using CMOS
160 video camera (Basler acA1300-200um, Basler AG, Ahrensburg, Germany) and analyzed by
161 computer-assisted sperm analysis (CASA, Sperm Class Analyzer version 6.3, Microptic,
162 Barcelona, Spain). Sperm total motility and hyperactivated motility was quantified simultaneously.
163 Over 200 motile sperm were analyzed for each trial, at least 3 biological replicates were performed
164 for each genotype. To track swimming trajectory, the sperm motility was videotaped at 50 fps. The
165 images were analyzed using Fiji software (Schindelin, Arganda-Carreras et al. 2012) by
166 assembling overlays of the flagellar traces generated by hyperstacking binary images of 20 frames
167 of 2 s movies coded in a gray intensity scale.

168 **Scanning Electron microscopy**

169 Sperm cells were attached on the glass coverslips and fixed with 2.5% glutaraldehyde (GA) in 0.1
170 M sodium cacodylate buffer (pH 7.4) for one hour at 4°C and post fixed in 2% osmium tetroxide
171 in 0.1 M cacodylate buffer (pH 7.4). The fixed samples were washed with 0.1 M cacodylate buffer
172 for 3 times and dehydrated through a series of ethanol to 100%. The samples were dried using a
173 300 critical point dryer with liquid carbon dioxide as transitional fluid. The coverslips with dried
174 samples were glued to aluminum stubs and sputter coated with 5 nm platinum using a Cressington
175 208HR (Ted Pella) rotary sputter coater. Prepared samples were imaged with Hitachi SU-70
176 scanning electron microscope (Hitachi High-Technologies).

177 **Transmitted electron microscopy**

178 Collected epididymal sperm cells were washed and pelleted by centrifugation and fixed in 2.5%
179 GA and 2% PFA in 0.1 M cacodylate buffer pH 7.4 for one hour at RT. Fixed sperm pellets were
180 rinsed with 0.1 M cacodylate buffer and spud down in 2% agar. The chilled blocks were trimmed,
181 rinsed in the 0.1 M cacodylate buffer, and replaced with 0.1% tannic acid in the buffer for one
182 hour. After rinsing in the buffer, the samples were post-fixed in 1% osmium tetroxide and 1.5%
183 potassium ferrocyanide in 0.1 M cacodylate buffer for one hour. The post-fixed samples were

184 rinsed in the cacodylate buffer and distilled water, followed by en bloc staining in 2% aqueous
185 uranyl acetate for one hour. Prepared samples were rinsed and dehydrated in an ethanol series to
186 100%. Dehydrated samples were infiltrated with epoxy resin Embed 812 (Electron Microscopy
187 Sciences), placed in silicone molds and baked for 24 hours at 60°C. The hardened blocks were
188 sectioned in 60 nm thickness using Leica UltraCut UC7. The sections were collected on grids
189 coated with formvar/carbon and contrast stained using 2% uranyl acetate and lead citrate. The
190 grids were imaged using FEI TecnaiBiotwin Transmission Electron Microscope (FEI, Hillsbroro,
191 OR) at 80 kV. Images were taken using MORADA CCD camera and iTEM (Olympus) software.

192 **Sperm Chromatin Dispersion Test (Halo Assay)**

193 Samples were diluted to the concentration of 5-10×10^6 cells/mL, then mixed with low-melting-
194 point aqueous agarose to obtain a final concentration of 0.7% agarose. 50 µl mixture was dispensed
195 onto a glass slide pre-coated with 0.65% standard agarose, then covered by a coverslip for
196 solidification at 4°C for 4 minutes. The coverslip was then removed carefully before the sample
197 was immersed into freshly prepared acid denaturation solution (0.08 N HCl) for 7 minutes,
198 neutralizing and lysing solution 1 (0.4 M Tris-HCl, 0.8M DTT, 1% SDS, 50 mM EDTA, pH 7.5)
199 for 10 min, and neutralizing and lysing solution 2 (0.4 M Tris-HCl, 2 M NaCl, 1% SDS, pH 7.5)
200 for 5 min at RT in sequence. The slide was then transferred to Tris-borate EDTA solution (90 mM
201 Tris-borate, 2 mM EDTA, pH 7.5) for 2 min, then dehydrated in sequential 70%, 90%, and 100%
202 EtOH (2 min each). After drying, the slide was stained with DAPI (2 ug/ml), then examined under
203 microscope as described above. The Halo size (diameter) was defined and classified into big (>17
204 µm), medium (between 12 and 17 µm) and small size (<12 µm).

205 **Acridine Orange Assay**

206 Sperm cells were smeared on glass slide until dry, followed by washing in PBS pH 7.2. 4%
207 paraformaldehyde (PFA) was used to fix cells for 15 min at RT, then covered by methanol for 5
208 min. washed with PBS for 5 min. The sample was incubated in RNAse A solution at 37°C for 30
209 minutes. Washing with PBS of pH 7.2 for 5 min was performed between each step. 0.1 M HCl
210 was used for DNA denaturation for 30-45 sec, followed by AO staining working solution for 2
211 min. The slide was ready for examination under fluorescence microscopy after washing gently and
212 drying.

213 **Mitochondrial Membrane Potential (ΔΨm) Measurement**

214 Epididymal sperm were attached on Delta T culture chamber coated with poly-D-Lysine (2 mg/mL)
215 or together with Cell-Tak for 30 min. Unattached sperm were removed by the gentle pipette wash.
216 Mitotracker deep red (working concentration 500 nM, ThermoFisher) was loaded in sperm for 30
217 min, followed by gentle rinse with HS or HEPES-buffered HTF medium H-HTF. All movies were
218 taken at 37°C by the pco.edge sCMOS camera equipped in Axio observer Z1 microscope (Carl
219 Zeiss). The data were analyzed by Zen (Blue).

220 **Quantification and statistical analysis**

221 Statistical analyses were performed using Student's t-test or one-way analysis of variance
222 (ANOVA) with Tukey post hoc test. Differences were considered significant at $*p < 0.05$, $**p <$
223 0.01, and $***p < 0.001$.

224 **Results**

225 ***Txnrd3*$^{-/-}$ sperm cells display defects in morphology and motility under capacitating conditions**

226 To understand why *Txnrd3*$^{-/-}$ males exhibit sub-fertility *in vivo* and *in vitro* (Dou et al., 2021), we
227 first examined sperm morphology and count from the cauda epididymis. The number of sperm
228 produced by *Txnrd3*$^{-/-}$ males was smaller than that from 2-3 months old heterozygous littermates
229 (Supplementary Figure 1A). Among them, some *Txnrd3*$^{-/-}$ sperm displayed hairpin formation
230 within midpiece, specifically evident after 90 min incubation under capacitating conditions (Figure
231 1A, B) whereas sperm bent around annulus were negligible in both wild type and *Txnrd3*$^{-/-}$ mice.
232 However, scanning electron microscopy (SEM) analysis did not reveal any gross abnormalities in
233 the sperm midpiece (Figure 1C).

234

235 Prompted by the capacitation-associated hairpin formation within midpiece, we next analyzed
236 sperm motility. Flagellar waveform analysis revealed that *Txnrd3*$^{-/-}$ sperm become stiff in the
237 midpiece and beat abnormally after incubating under capacitating conditions (Figure 1D,
238 Supplementary Figure 1C and Video S1). Accordingly, CASA analysis found that overall motility
239 of *Txnrd3*$^{-/-}$ sperm was diminished (Supplementary Figure 1B). By contrast, hyperactivated
240 motility is not significantly affected, likely because the *Txnrd3*$^{-/-}$ sperm that are not bent still
241 develop hyperactivated motility. To better understand the effect of TXNRD3 deficiency on free
242 swimming pattern, sperm cells were placed in 0.3% methylcellulose which mimics viscous
243 environment in the female reproductive tract. Swimming trajectory traced by time-lapse video
244 microscope demonstrated that *Txnrd3*$^{-/-}$ sperm move a shorter distance at a given time after

245 capacitation (Figure 1E and Video S2), suggesting that the hairpin prevents them from swimming
246 as efficiently as wild type sperm.
247
248 **Absence of TXNRD3 affects the redox state of both head and tail of sperm**
249 TXNRD3 is enriched in testis but not readily detected in epididymis (Su, Novoselov et al. 2005).
250 Our analysis of the publicly available scRNA-seq database (Speir, Bhaduri et al. 2020) found that
251 *Txrnd3* mRNA expression is higher in spermatogonia and spermatocytes but much less in
252 spermatids (Supplementary Figure 2). We hypothesize that diminishing TXNRD3 mRNA and
253 protein levels in epididymal sperm along the tract underlies the changes in the overall redox state
254 of proteins during epididymal maturation and capacitation of sperm. Thus, we examined the
255 changes in the TXNRD3 protein levels and found decreasing amount of TXNRD3 in sperm during
256 their descent through epididymis (Figure 2A, B). We next examined the distribution and the extent
257 of protein thiol modification in the absence of TXNRD3 by labeling epididymal sperm cells with
258 ThiolTracker that reacts with reduced thiols (free "-SH") irreversibly. Consistent with TXNRD3
259 levels from caput to cauda, wild type sperm from caput region exhibited strong fluorescence over
260 the entire cell whereas corpus and cauda sperm displayed gradually diminishing fluorescence
261 intensity, more noticeably in the head (Figure 2C, D). These results are in line with the previously
262 reported more disulfide bond formation in sperm during their transit along the male reproductive
263 tract (Dias, López et al. 2014).
264
265 Using ThiolTracker or BODIPY-NEM, another thiol-reactive dye, we found that in the absence of
266 TXNRD3, free thiol contents is further decreased modestly, yet significantly, in cauda sperm
267 (Figure 2C, D and Supplementary Figure 3A). It is possible that other reductases function
268 redundantly and compensate the loss of TXNRD3; both TXNRD1 and TXNRD2 proteins are
269 detected in wild type and *Txnrd3*$^{-/-}$ sperm (Supplementary Figure 3D). As sperm proteins were
270 found more oxidized in cauda than in caput, we speculate that the efficiency of protein extraction
271 can be affected by the overall redox status. Indeed, when we used urea instead of SDS to examine
272 the protein levels of TXNRD3 from caput, corpus, and cauda sperm, we did not observe significant
273 difference (Figure 2E), suggesting that TXNRD3 itself is likely a substrate of thioredoxin system
274 during epididymal maturation.
275

276 Sperm midpiece harbors compartmentalized mitochondria(Skinner 2018) (see also Figure 1C). As
277 *Txnrd3*$^{-/-}$ sperm specifically exhibit the hairpin formation within the midpiece, next we tested
278 whether the TXNRD3 loss-of-function affects the redox states of mitochondrial proteinsmore
279 specifically. In the SDS extracted fraction, the protein level of glutathione peroxidase 4 (GPX4) -
280 a mitochondrial structural protein and potential substrate of TXNRD3 (Ursini, Heim et al. 1999,
281 Su, Novoselov et al. 2005) – is much lower in the cauda sperm just as seen for TXNRD3 (Figure
282 2A, B and Supplementary Figure 3B,C). By contrast, urea readily extracted GPx4 even from cauda
283 sperm (Figure 2F, *supernatant*), indicating that GPx4 becomes likely more oxidized, thus SDS-
284 insoluble during epididymal transit. Intriguingly, we observed a urea-insoluble GPx4 fraction not
285 in wild type but in *Txnrd3*$^{-/-}$ cauda sperm when the pellet was further solubilized by guanidine after
286 urea (Figure 2F, *pellet*). Other non-structural but membrane proteins localized in sperm
287 mitochondria such as ANT4, P2X2 and TOM20 and the other two thioredoxin reductases -
288 TXNRD1 and TXNRD2 - were well solubilized in all detergents tested (Figure 2F and
289 Supplementary Figure 3D). Taken together, TXNRD3 is involved in redox regulation of sperm
290 proteins during epididymal transition.
291
292 **Capacitation-associated oxidation is deregulated in *Txnrd3*$^{-/-}$ sperm (chromatin organization)**
293 It has been known that redox signaling is involved in sperm capacitation (O'Flaherty 2015). We
294 next examined how free thiol levels change during sperm capacitation. Under capacitating
295 conditions, wild type sperm were less reactive with ThiolTracker, particularly in the head, whereas
296 *Txnrd3*$^{-/-}$ sperm was not reactive regardless (Figure 3A). These results suggest that sperm proteins
297 were more oxidized in the absence of TXNRD3 during sperm maturation, which remain relatively
298 stable during capacitation. To test this idea, we examined protein oxidation levels by detecting
299 carbonyl groups inserted into proteins. Incubating sperm under capacitating conditions
300 dramatically increase sperm protein carbonylation, suggesting active oxidative reactions occur.
301 The protein oxidation level is further enhanced in *Txnrd3*$^{-/-}$ sperm (Figure 3B and Supplementary
302 Figure 4).
303
304 As the free thiol level changes were most dramatic in the head, we next investigated the loss of
305 TXNRD3 function on sperm chromatin organization. We examined the extent of DNA integrity
306 by halo assay where radial dispersion of the DNA fragments from the nucleus was measured upon

307 artificial acid denaturation; the bigger the halo size is, the less damaged DNA fragment is present
308 (Fernández, Muriel et al. 2003, Chohan, Griffin et al. 2006, Tandara, Bajić et al. 2014). Intriguingly,
309 *Txnrd3*$^{-/-}$ sperm resist the denaturation better, developing smaller halos than those of wild type
310 sperm (Figure 4). This result suggests more damaged, double stranded DNA fragments are in the
311 nucleus in the absence of TXNRD3, likely due to more DNA fragments crosslinked to proteins.
312 The nuclei of sperm incubated under capacitating conditions, develop smaller halos in both wild
313 type and *Txnrd3*$^{-/-}$ sperm (Figure 4), suggesting the oxidative conditions. We further evaluated the
314 altered resistance of DNA to acid denaturation by acridine orange (AO) assay; AO produces
315 different emission when bound to single vs. double stranded DNA. Likewise, we observed that
316 double-strand DNAs in both nucleus and mitochondria in capacitated *Txnrd3*$^{-/-}$ sperm are more
317 stable and resistant to acid denaturation (Supplementary Figure 5). Taken together, antioxidant
318 capacity in *Txnrd3*$^{-/-}$ sperm is lower than wild type sperm; TXNRD3 participates redox regulation
319 of epididymal sperm maturation, protecting mitochondrial structure and chromatin from oxidative
320 damage during sperm capacitation.
321
322 **Lack of TXNRD3 dysregulates capacitation-induced remodeling of sperm mitochondrial**
323 **ultrastructure**
324 To maintain motility and support capacitation after ejaculation, mammalian sperm utilize
325 nutrient molecules in the seminal plasma and in the female reproductive tract environment to
326 generate energy (Visconti 2012). As terminally differentiated and highly polarized cells, sperm
327 uniquely compartmentalize metabolic pathways in the flagella: the glycolytic enzymes are
328 specifically localized in the principal piece and the mitochondrial oxidative phosphorylation
329 (OXPHOS) occurs in the midpiece (Skinner 2018). A classic view on mouse sperm bioenergetics
330 has been that glycolysis is the main metabolic pathway to support tyrosine phosphorylation and
331 hyperactivation whereas both glycolytic and OXPHOS are functional (Travis, Jorgez et al. 2001,
332 Mukai and Okuno 2004, Goodson, Qiu et al. 2012). Intriguingly, our transmission electron
333 microscopy (TEM) analysis revealed that mitochondria display more well-defined cristae after
334 incubating under capacitating conditions (Figure 5A, B). Dimerization of the V-like shaped
335 mitochondrial ATPase and its self-assembly into rows drives the cristae organization and
336 determines respiratory efficiency (Dudkina, Sunderhaus et al. 2006, Strauss, Hofhaus et al. 2008,
337 Cogliati, Frezza et al. 2013, Blum, Hahn et al. 2019). Thus, our results suggest that capacitation

338 increases mitochondrial activity in mouse sperm. In addition, we observed that capacitation
339 induces electron-dense cores in the mitochondrial matrix of capacitated sperm cells (Figure 5A,
340 B). Notably, *Txnrd3*$^{-/-}$ sperm developed significantly more dense cores than wild type sperm
341 regardless of capacitation status. As similar dense cores were previously reported in *Pmca4*$^{-/-}$
342 sperm that might potentially experience Ca^{2+} overload (Okunade, Miller et al. 2004), this result
343 suggests that redox pathways might be involved in Ca^{2+} signaling regulation during sperm
344 capacitation.
345
346 ***Txnrd3*$^{-/-}$ sperm lose control of mitochondrial membrane hyperpolarization**
347 Mitochondrial membrane potential (ΔΨm) is an essential driving force for oxidative
348 phosphorylation. To better understand how mitochondrial activity changes during sperm
349 capacitation and the loss-of-function effect of TXNRD3 on this process, we performed functional
350 imaging to probe ΔΨm using MitoTracker DeepRed, a fluorescent dye specifically taken up by
351 mitochondria in live cells according to ΔΨm (Lugli, Troiano et al. 2005, Zhou, Yazdi et al. 2011,
352 Greene, Grenier et al. 2012). The decreased fluorescence intensity of MitoTracker DeepRed
353 indicates mitochondrial depolarization. In agreement of higher mitochondrial activity during
354 capacitation, dissipated ΔΨm by antimycin A - an inhibitor of oxidative phosphorylation - is
355 greater in wild type sperm incubated under capacitating conditions (Figure 6 and Supplementary
356 Figure 6). Under non-capacitating conditions, we find that ΔΨm is not significantly different from
357 wild type to that of *Txnrd3*$^{-/-}$ sperm. Under capacitating conditions, however, we found two distinct
358 populations among TXNRD3-deficient sperm in terms of ΔΨm (Figure 6 and Supplementary
359 Figure 6); one group did not show any change in the fluorescent intensity of the dye upon
360 antimycin A, suggesting reduced or no mitochondrial activity (red trace) whereas the other group
361 exhibited ΔΨm at a similar level to wild type sperm. These results illustrate that loss of TXNRD3
362 dysregulates the capacitation-associated remodeling of mitochondrial function in mouse sperm.

363 **Discussion**

364 **Evidence that TXNRD3 mediates sperm functions and redox regulation in male fertility**
365 In the accompanying manuscript, we have shown that *Txnrd3*$^{-/-}$ male mice reduced fertility *in vivo*
366 and *in vitro* (Dou et al., 2021). The findings in this study further demonstrate that the subfertility
367 likely results from the combinatorial effects of defective chromatin organization, capacitation-

368 induced tail bending within the midpiece. The high degree of sperm DNA fragmentation was
369 reported to correlate with low fertilization rates, embryo quality and pregnancy after IVF and
370 intracytoplasmic sperm injection (Loft, Kold-Jensen et al. 2003, Tandara, Bajić et al. 2014).The
371 bent tail would force the head backwards, opposite to the swimming direction of the sperm.
372 Additionally, TXNRD3 in sperm is gradually oxidized during epididymal transit, which is
373 consistent with reduced free thiol group levels in cells along the epididymal tract. Therefore, the
374 main place of TXNRD3 activity is likely to be during spermatogenesis in testis and epididymal
375 maturation rather than fertilization process. Moderated changes in the free thiol levels or redox
376 status in the *Txnrd3*$^{-/-}$ sperm may be due to functional redundancy of other reductases in other
377 systems that partly compensate for the loss of TXNRD3. Alternatively, the extent of the overall
378 redox status is only marginally changed in the absence of TXNRD3, but the pattern of disulfide
379 bond formation could be jumbled, sufficient to make *Txnrd3*$^{-/-}$ sperm vulnerable to capacitation-
380 associated oxidative damage.
381
382 **Mitochondrial function and metabolism regulation during capacitation**
383 Mitochondria is a key organelle still preserved in the fully differentiated spermatozoa. Previous
384 knock-out studies of sperm-specific glyceraldehyde 3-phosphate dehydrogenase and
385 phosphoglycerate kinase 2 have identified glycolysis as the main source of ATP to sustain the
386 motility of mouse spermatozoa (Miki, Qu et al. 2004, Danshina, Geyer et al. 2010). Because
387 OXPHOS yields more ATP per mol of glucose than glycolysis, the discordant contribution of the
388 two metabolic pathways to provide the energy for mouse sperm motility has been an unresolved
389 puzzle for a long time. A comparative study revealed that sperm of closely related mouse species
390 with higher oxygen consumption rate were able to produce higher amounts of ATP, achieving
391 higher swimming velocities (Tourmente, Villar-Moya et al. 2015).
392
393 For the first time in our knowledge, here we report that capacitation induces sperm mitochondria
394 to form more defined cristae (Figure 5). As ATPase dimerization and self-assembly drives to
395 cristae formation (Dudkina, Sunderhaus et al. 2006, Strauss, Hofhaus et al. 2008, Blum, Hahn et
396 al. 2019), this result indicates that capacitation enhances OXPHOS pathway to supply additional
397 ATP. The higher metabolic activity in capacitating sperm is further supported by our observation
398 of more hyperpolarized mitochondrial membrane potential ($\Delta\Psi m$) (Figure 6), an indication of

399 protonmotive force and mitochondrial function. Consistently, a recent study reported accelerated
400 oxygen consumption rate in capacitated sperm (Balbach, Gervasi et al. 2020).
401
402 Interestingly, we observed that significant portion of TXNRD3-deficient sperm not only fail to
403 maintain ΔΨm but also develop a more apparent electron-dense core in the mitochondrial matrix.
404 As a condensed mitochondrial matrix was observed in absence of plasma membrane Ca^{2+}-ATPase
405 4 (Okunade, Miller et al. 2004), this result may indicate that calcium is overloaded in *Txnrd3*$^{-/-}$
406 sperm mitochondria during sperm capacitation. Whether the TXNRD3-deficient sperm cells that
407 cannot maintain ΔΨm are the same sperm populations with the electron-dense core requires further
408 work. The small cytosol volume in mature sperm makes it difficult to achieve spatial resolution
409 specific to mitochondria Ca^{2+} imaging with currently available Ca^{2+} dyes. Generation of a mouse
410 model expressing a genetically encoded Ca^{2+} indicator specifically targeted to sperm mitochondria
411 will help to directly address the functional relationship of redox regulation of mitochondria
412 dynamics in Ca^{2+} homeostasis and sperm metabolism during capacitation.
413
414 In summary, our study investigated the TXNRD3 function and potential cellular mechanisms in
415 sperm maturation and male fertility. The absence of TXNRD3 likely deregulate redox state of
416 sperm chromatin and mitochondrial structure proteins during capacitation, resulting in distinct
417 hairpin-like bending and defective mitochondrial respiration; the loss-of-function prevents *Txnrd3*$^{-}$
418 $^{/-}$ sperm from properly positioning to penetrate the eggs and compromising efficient ATP
419 production. *Txnrd3*$^{-/-}$ mice are fertile in controlled laboratory environment without limitation of
420 resource and male competition. Yet our findings from *in vitro* experiments shows that TXNRD3
421 and thioredoxin system contribute to sperm function and male reproduction. This new knowledge
422 could help the conditions for assisted reproductive technology in clinics.

423 **Conflict of Interest**

424 The authors declare no competing interests.

425 **Author Contributions**

426 J.-J.C. and V.N.G. conceived the study. J.-J.C. oversaw the project. J.-J.C. and H.W. designed the
427 experiments. H.W., Q.D., and J.-J.C. performed experiments. K.J. and J.C. analyzed scRNAseq

database. H.W. prepared the figures and H.W. and J.-J.C wrote the initial draft of the manuscript. H.W., V.N.G. and J.-J.C. edited the manuscript with input from all other authors in the final version.

Funding

This work was funded by (to be added) to V.N.D. and the start-up funds from Yale School of Medicine and the National Institutes of Health (R01HD096745) to J.-J.C.

Acknowledgments

We thank the Yale Center for Cellular and Molecular Imaging for assistance in scanning electron microscopy, Jae Yeon Hwang for help in TEM analysis of sperm mitochondria, and Xiaofang Huang for initial analysis of free thiol measurement.

Reference

Arnér, E. S. and A. Holmgren (2000). "Physiological functions of thioredoxin and thioredoxin reductase." Eur J Biochem **267**(20): 6102-6109.

Balbach, M., M. G. Gervasi, D. M. Hidalgo, P. E. Visconti, L. R. Levin and J. Buck (2020). "Metabolic changes in mouse sperm during capacitation†." Biol Reprod **103**(4): 791-801.

Blum, T. B., A. Hahn, T. Meier, K. M. Davies and W. Kühlbrandt (2019). "Dimers of mitochondrial ATP synthase induce membrane curvature and self-assemble into rows." Proc Natl Acad Sci U S A **116**(10): 4250-4255.

Chabory, E., C. Damon, A. Lenoir, G. Kauselmann, H. Kern, B. Zevnik, C. Garrel, F. Saez, R. Cadet, J. Henry-Berger, M. Schoor, U. Gottwald, U. Habenicht, J. R. Drevet and P. Vernet (2009). "Epididymis seleno-independent glutathione peroxidase 5 maintains sperm DNA integrity in mice." J Clin Invest **119**(7): 2074-2085.

Chohan, K. R., J. T. Griffin, M. Lafromboise, C. J. De Jonge and D. T. Carrell (2006). "Comparison of chromatin assays for DNA fragmentation evaluation in human sperm." J Androl **27**(1): 53-59.

Chung, J. J., K. Miki, D. Kim, S. H. Shim, H. F. Shi, J. Y. Hwang, X. Cai, Y. Iseri, X. Zhuang and D. E. Clapham (2017). "CatSperζ regulates the structural continuity of sperm Ca(2+) signaling domains and is required for normal fertility." Elife **6**.

Chung, J. J., B. Navarro, G. Krapivinsky, L. Krapivinsky and D. E. Clapham (2011). "A novel gene required for male fertility and functional CATSPER channel formation in spermatozoa." Nat Commun **2**: 153.

Chung, J. J., S. H. Shim, R. A. Everley, S. P. Gygi, X. Zhuang and D. E. Clapham (2014). "Structurally distinct Ca(2+) signaling domains of sperm flagella orchestrate tyrosine phosphorylation and motility." Cell **157**(4): 808-822.

Cogliati, S., C. Frezza, M. E. Soriano, T. Varanita, R. Quintana-Cabrera, M. Corrado, S. Cipolat, V. Costa, A. Casarin, L. C. Gomes, E. Perales-Clemente, L. Salviati, P. Fernandez-Silva, J. A. Enriquez and L. Scorrano (2013). "Mitochondrial cristae shape determines respiratory chain supercomplexes assembly and respiratory efficiency." Cell **155**(1): 160-171.

Conrad, M., C. Jakupoglu, S. G. Moreno, S. Lippl, A. Banjac, M. Schneider, H. Beck, A. K. Hatzopoulos, U. Just, F. Sinowatz, W. Schmahl, K. R. Chien, W. Wurst, G. W. Bornkamm and M. Brielmeier (2004). "Essential

466 role for mitochondrial thioredoxin reductase in hematopoiesis, heart development, and heart function."
467 Mol Cell Biol **24**(21): 9414-9423.
468 Danshina, P. V., C. B. Geyer, Q. Dai, E. H. Goulding, W. D. Willis, G. B. Kitto, J. R. McCarrey, E. M. Eddy and
469 D. A. O'Brien (2010). "Phosphoglycerate kinase 2 (PGK2) is essential for sperm function and male fertility
470 in mice." Biol Reprod **82**(1): 136-145.
471 Dias, G. M., M. L. López, A. T. Ferreira, D. A. Chapeaurouge, A. Rodrigues, J. Perales and C. A. Retamal
472 (2014). "Thiol-disulfide proteins of stallion epididymal spermatozoa." Anim Reprod Sci **145**(1-2): 29-39.
473 Dudkina, N. V., S. Sunderhaus, H. P. Braun and E. J. Boekema (2006). "Characterization of dimeric ATP
474 synthase and cristae membrane ultrastructure from Saccharomyces and Polytomella mitochondria." FEBS
475 Lett **580**(14): 3427-3432.
476 Dou, Q., ..Hwang, J.Y., … Chung, J.-J. Gladyshev, V.N. (2021) "Title TBD" to be posted to bioRxiv
477 Fernández, J. L., L. Muriel, M. T. Rivero, V. Goyanes, R. Vazquez and J. G. Alvarez (2003). "The sperm
478 chromatin dispersion test: a simple method for the determination of sperm DNA fragmentation." J Androl
479 **24**(1): 59-66.
480 Finak, G., A. McDavid, M. Yajima, J. Deng, V. Gersuk, A. K. Shalek, C. K. Slichter, H. W. Miller, M. J. McElrath,
481 M. Prlic, P. S. Linsley and R. Gottardo (2015). "MAST: a flexible statistical framework for assessing
482 transcriptional changes and characterizing heterogeneity in single-cell RNA sequencing data." Genome
483 Biol **16**: 278.
484 Gervasi, M. G. and P. E. Visconti (2017). "Molecular changes and signaling events occurring in spermatozoa
485 during epididymal maturation." Andrology **5**(2): 204-218.
486 Goodson, S. G., Y. Qiu, K. A. Sutton, G. Xie, W. Jia and D. A. O'Brien (2012). "Metabolic substrates exhibit
487 differential effects on functional parameters of mouse sperm capacitation." Biol Reprod **87**(3): 75.
488 Greene, A. W., K. Grenier, M. A. Aguileta, S. Muise, R. Farazifard, M. E. Haque, H. M. McBride, D. S. Park
489 and E. A. Fon (2012). "Mitochondrial processing peptidase regulates PINK1 processing, import and Parkin
490 recruitment." EMBO Rep **13**(4): 378-385.
491 Henkel, R., E. Kierspel, T. Stalf, C. Mehnert, R. Menkveld, H. R. Tinneberg, W. B. Schill and T. F. Kruger
492 (2005). "Effect of reactive oxygen species produced by spermatozoa and leukocytes on sperm functions
493 in non-leukocytospermic patients." Fertil Steril **83**(3): 635-642.
494 Hermann, B. P., K. Cheng, A. Singh, L. Roa-De La Cruz, K. N. Mutoji, I. C. Chen, H. Gildersleeve, J. D. Lehle,
495 M. Mayo, B. Westernstroer, N. C. Law, M. J. Oatley, E. K. Velte, B. A. Niedenberger, D. Fritze, S. Silber, C.
496 B. Geyer, J. M. Oatley and J. R. McCarrey (2018). "The Mammalian Spermatogenesis Single-Cell
497 Transcriptome, from Spermatogonial Stem Cells to Spermatids." Cell Rep **25**(6): 1650-1667 e1658.
498 Holmgren, A. (1980). "Pyridine nucleotide - disulfide oxidoreductases." Experientia Suppl **36**: 149-180.
499 Jakupoglu, C., G. K. Przemeck, M. Schneider, S. G. Moreno, N. Mayr, A. K. Hatzopoulos, M. H. de Angelis,
500 W. Wurst, G. W. Bornkamm, M. Brielmeier and M. Conrad (2005). "Cytoplasmic thioredoxin reductase is
501 essential for embryogenesis but dispensable for cardiac development." Mol Cell Biol **25**(5): 1980-1988.
502 Kao, S. H., H. T. Chao, H. W. Chen, T. I. S. Hwang, T. L. Liao and Y. H. Wei (2008). "Increase of oxidative
503 stress in human sperm with lower motility." Fertil Steril **89**(5): 1183-1190.
504 Korsunsky, I., N. Millard, J. Fan, K. Slowikowski, F. Zhang, K. Wei, Y. Baglaenko, M. Brenner, P. R. Loh and
505 S. Raychaudhuri (2019). "Fast, sensitive and accurate integration of single-cell data with Harmony." Nat
506 Methods **16**(12): 1289-1296.
507 Loft, S., T. Kold-Jensen, N. H. Hjollund, A. Giwercman, J. Gyllemborg, E. Ernst, J. Olsen, T. Scheike, H. E.
508 Poulsen and J. P. Bonde (2003). "Oxidative DNA damage in human sperm influences time to pregnancy."
509 Hum Reprod **18**(6): 1265-1272.
510 Lugli, E., L. Troiano, R. Ferraresi, E. Roat, N. Prada, M. Nasi, M. Pinti, E. L. Cooper and A. Cossarizza (2005).
511 "Characterization of cells with different mitochondrial membrane potential during apoptosis." Cytometry
512 A **68**(1): 28-35.

513 Miki, K., W. Qu, E. H. Goulding, W. D. Willis, D. O. Bunch, L. F. Strader, S. D. Perreault, E. M. Eddy and D. A.
514 O'Brien (2004). "Glyceraldehyde 3-phosphate dehydrogenase-S, a sperm-specific glycolytic enzyme, is
515 required for sperm motility and male fertility." Proc Natl Acad Sci U S A **101**(47): 16501-16506.
516 Mukai, C. and M. Okuno (2004). "Glycolysis plays a major role for adenosine triphosphate
517 supplementation in mouse sperm flagellar movement." Biol Reprod **71**(2): 540-547.
518 Mustacich, D. and G. Powis (2000). "Thioredoxin reductase." Biochem J **346 Pt 1**(Pt 1): 1-8.
519 Nalvarte, I., A. E. Damdimopoulos, C. Nystöm, T. Nordman, A. Miranda-Vizuete, J. M. Olsson, L. Eriksson,
520 M. Björnstedt, E. S. Arnér and G. Spyrou (2004). "Overexpression of enzymatically active human cytosolic
521 and mitochondrial thioredoxin reductase in HEK-293 cells. Effect on cell growth and differentiation." J Biol
522 Chem **279**(52): 54510-54517.
523 O'Flaherty, C. (2015). "Redox regulation of mammalian sperm capacitation." Asian J Androl **17**(4): 583-
524 590.
525 Okunade, G. W., M. L. Miller, G. J. Pyne, R. L. Sutliff, K. T. O'Connor, J. C. Neumann, A. Andringa, D. A.
526 Miller, V. Prasad, T. Doetschman, R. J. Paul and G. E. Shull (2004). "Targeted ablation of plasma membrane
527 Ca2+-ATPase (PMCA) 1 and 4 indicates a major housekeeping function for PMCA1 and a critical role in
528 hyperactivated sperm motility and male fertility for PMCA4." J Biol Chem **279**(32): 33742-33750.
529 Schindelin, J., I. Arganda-Carreras, E. Frise, V. Kaynig, M. Longair, T. Pietzsch, S. Preibisch, C. Rueden, S.
530 Saalfeld, B. Schmid, J. Y. Tinevez, D. J. White, V. Hartenstein, K. Eliceiri, P. Tomancak and A. Cardona (2012).
531 "Fiji: an open-source platform for biological-image analysis." Nat Methods **9**(7): 676-682.
532 Skinner, M. K. (2018). Encyclopedia of Reproduction, Elsevier Science.
533 Speir, M. L., A. Bhaduri, N. S. Markov, P. Moreno, T. J. Nowakowski, I. Papatheodorou, A. A. Pollen, L.
534 Seninge, W. J. Kent and M. Haeussler (2020). "UCSC Cell Browser: Visualize Your Single-Cell Data." bioRxiv:
535 2020.2010.2030.361162.
536 Strauss, M., G. Hofhaus, R. R. Schröder and W. Kühlbrandt (2008). "Dimer ribbons of ATP synthase shape
537 the inner mitochondrial membrane." Embo j **27**(7): 1154-1160.
538 Stuart, T., A. Butler, P. Hoffman, C. Hafemeister, E. Papalexi, W. M. Mauck, 3rd, Y. Hao, M. Stoeckius, P.
539 Smibert and R. Satija (2019). "Comprehensive Integration of Single-Cell Data." Cell **177**(7): 1888-1902
540 e1821.
541 Su, D., S. V. Novoselov, Q. A. Sun, M. E. Moustafa, Y. Zhou, R. Oko, D. L. Hatfield and V. N. Gladyshev (2005).
542 "Mammalian selenoprotein thioredoxin-glutathione reductase. Roles in disulfide bond formation and
543 sperm maturation." J Biol Chem **280**(28): 26491-26498.
544 Sullivan, R. and R. Mieusset (2016). "The human epididymis: its function in sperm maturation." Hum
545 Reprod Update **22**(5): 574-587.
546 Sun, Q. A., L. Kirnarsky, S. Sherman and V. N. Gladyshev (2001). "Selenoprotein oxidoreductase with
547 specificity for thioredoxin and glutathione systems." Proc Natl Acad Sci U S A **98**(7): 3673-3678.
548 Tandara, M., A. Bajić, L. Tandara, L. Bilić-Zulle, M. Šunj, V. Kozina, T. Goluža and M. Jukić (2014). "Sperm
549 DNA integrity testing: big halo is a good predictor of embryo quality and pregnancy after conventional
550 IVF." Andrology **2**(5): 678-686.
551 Tourmente, M., P. Villar-Moya, E. Rial and E. R. Roldan (2015). "Differences in ATP Generation Via
552 Glycolysis and Oxidative Phosphorylation and Relationships with Sperm Motility in Mouse Species." J Biol
553 Chem **290**(33): 20613-20626.
554 Travis, A. J., C. J. Jorgez, T. Merdiushev, B. H. Jones, D. M. Dess, L. Diaz-Cueto, B. T. Storey, G. S. Kopf and
555 S. B. Moss (2001). "Functional relationships between capacitation-dependent cell signaling and
556 compartmentalized metabolic pathways in murine spermatozoa." J Biol Chem **276**(10): 7630-7636.
557 Ursini, F., S. Heim, M. Kiess, M. Maiorino, A. Roveri, J. Wissing and L. Flohé (1999). "Dual function of the
558 selenoprotein PHGPx during sperm maturation." Science **285**(5432): 1393-1396.

559 van Dijk, D., R. Sharma, J. Nainys, K. Yim, P. Kathail, A. J. Carr, C. Burdziak, K. R. Moon, C. L. Chaffer, D.
560 Pattabiraman, B. Bierie, L. Mazutis, G. Wolf, S. Krishnaswamy and D. Pe'er (2018). "Recovering Gene
561 Interactions from Single-Cell Data Using Data Diffusion." Cell **174**(3): 716-729 e727.
562 Vernet, P., R. J. Aitken and J. R. Drevet (2004). "Antioxidant strategies in the epididymis." Mol Cell
563 Endocrinol **216**(1-2): 31-39.
564 Visconti, P. E. (2012). "Sperm bioenergetics in a nutshell." Biol Reprod **87**(3): 72.
565 Zhou, R., A. S. Yazdi, P. Menu and J. Tschopp (2011). "A role for mitochondria in NLRP3 inflammasome
566 activation." Nature **469**(7329): 221-225.

567

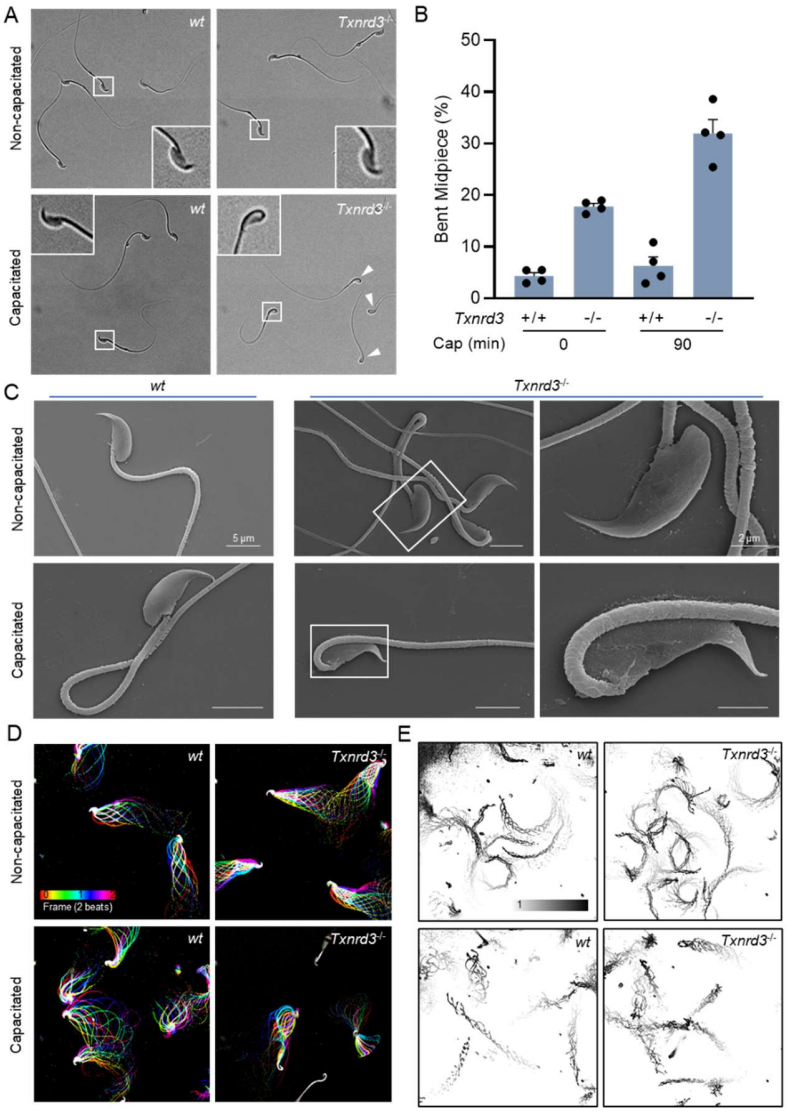

Figure 1. TXNRD3-deficient sperm are morphologically abnormal with impaired hyperactivated motility. (**A**) TXNRD3-deficient sperm exhibit abnormal hairpin morphology incubating under capacitation conditions. (**B**) Quantification of abnormal hairpin morphology from **A**. Mean ± SEM, n = X each group. $^{**}p < 0.01$ (**C**) Representative scanning electron microscopy (SEM) images of cauda epididymal sperm. (**C**) Aligned flagellar waveform traces. Sperm cells were examined 0 min and 90 min after incubation in capacitating conditions to induce hyperactivation. Representative traces of single spermatozoa from *wt* and *Txnrd3*$^{-/-}$ are shown. (**D**) Free swimming trajectory analysis.

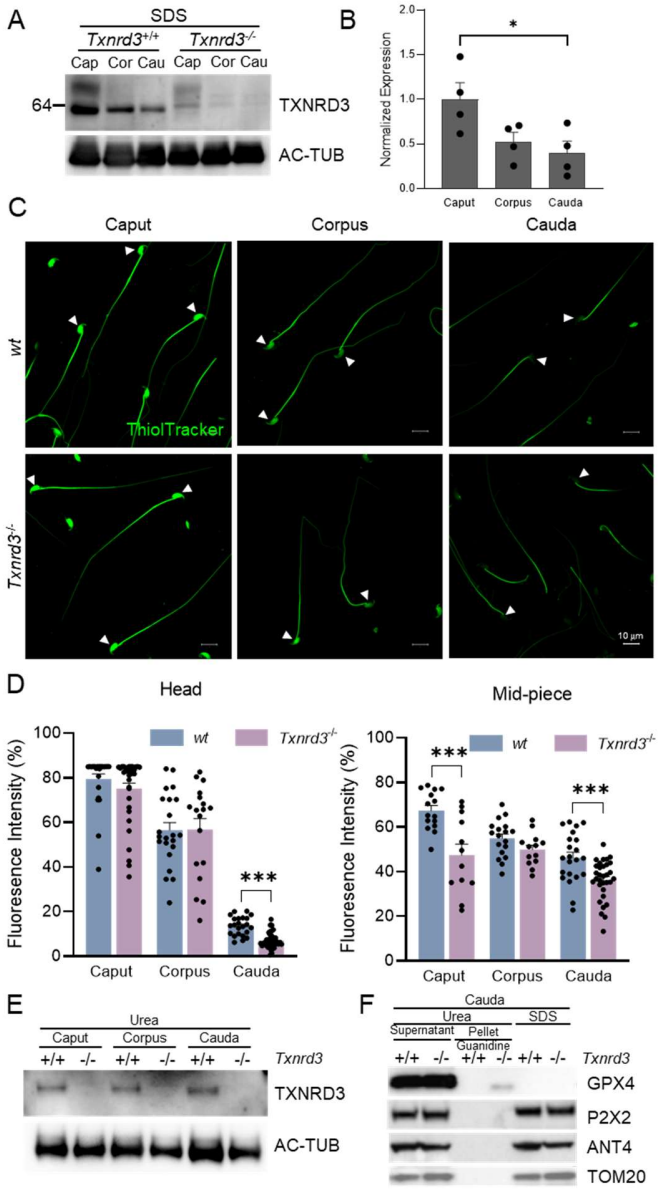

577

578 **Figure 2. Free thiol level and oxidative status is altered in *Txnrd3*$^{-/-}$ spermatozoa.** (**A**)
579 TXNRD3 expression decreased in concert with sperm maturation in epididymis. (**B**)
580 Quantification of TXNRD3 expression from (A). (**C**) Free thiol groups level in epididymal sperm
581 from *wt* and *Txnrd3*$^{-/-}$. Spermatozoa isolated from the caput, corpus and cauda epididymis were
582 incubated with ThiolTracker. (**D**) Relative quantification of free thiol level in sperm head and
583 midpiece. (**E**) TXNRD3 are equally extracted by urea from cauda sperm. (**F**) GPx4, a potential
584 TXNRD3 substrate candidate, exhibited stronger resistance to lysis buffer when absence of
585 TXNRD3.

586

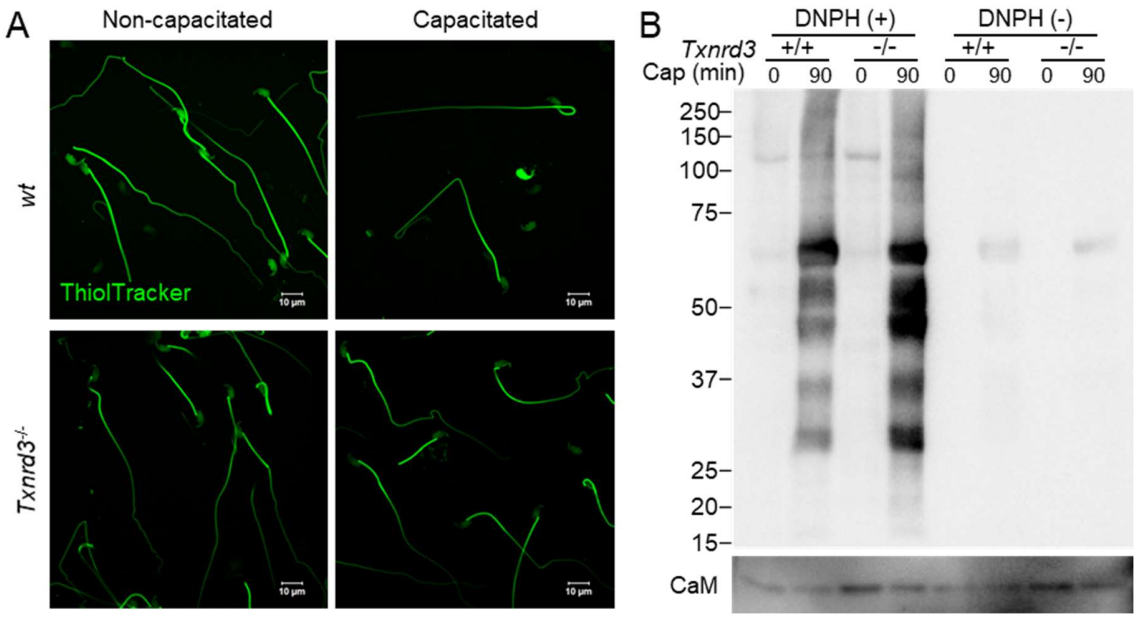

Figure 3. TXNRD3-deficient sperm undergo more oxidation after capacitation. (**A**) Free thiol groups level indicated with ThiolTracker in cauda epididymal sperm from wide type and *Txnrd3*$^{-/-}$ before and after 90 min capacitating condition. (**B**) Protein carbonylation level in both wide type and *Txnrd3*$^{-/-}$ sperm before and after capacitation.

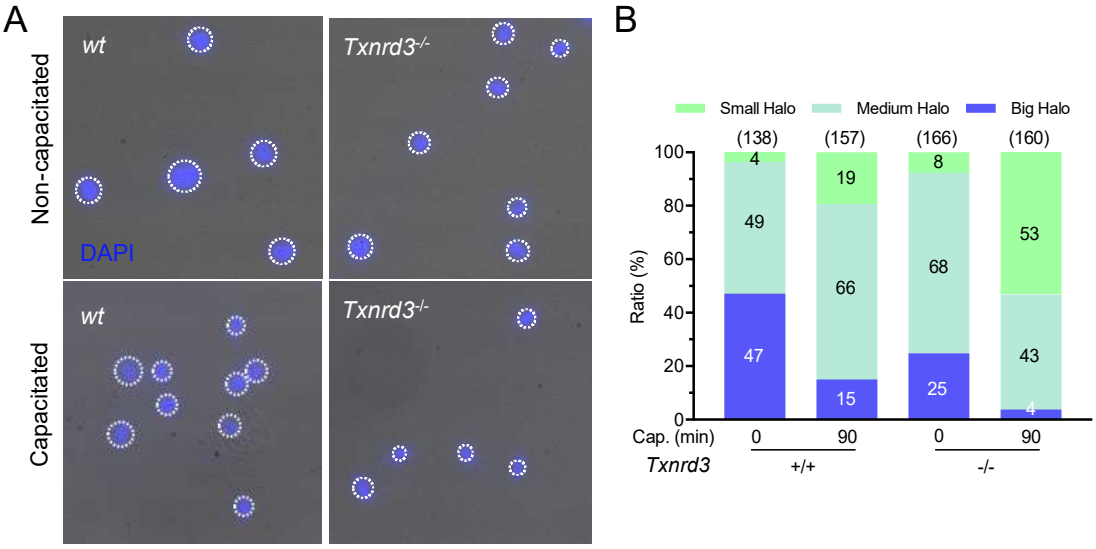

593

594 **Figure 4. TXNRD3-deficient sperm are more stable and resistant to acid denaturation after**
595 **capacitation.** (**A**) Sperm chromatin dispersion test show smaller halo in *Txnrd3*$^{-/-}$ sperm than in
596 *wt* sperm during capacitation, indicating extensive fragmented DNA after acid denaturation during
597 the assay procedure. DAPI (Blue). (**B**) Quantification of various halo size from WT and *Txnrd3*$^{-/-}$
598 sperm before and after capacitation. Based on sperm head size (~8 µm), halo sizes which are <12
599 µm (50% larger), <17 µm (100% larger) and >17 µm are divided into small, medium and big,
600 respectively.

601

602

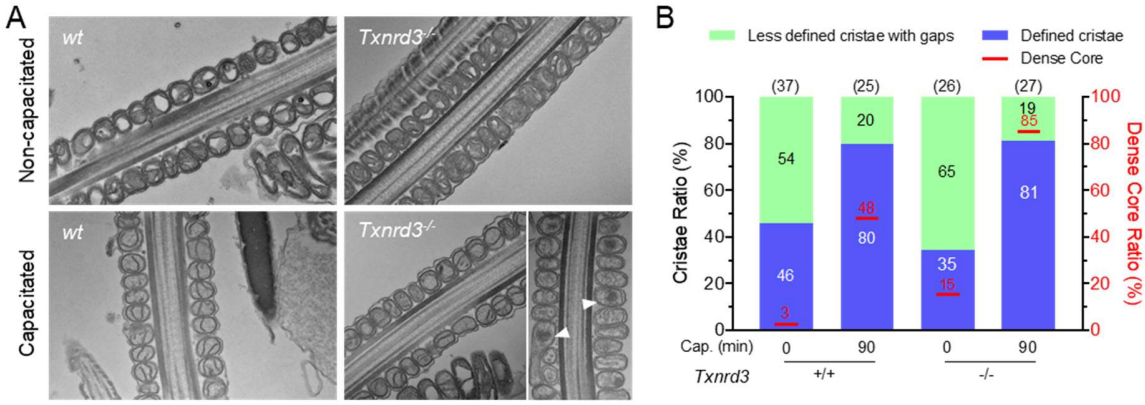

603 **Figure 5. Ultrastructural analysis of epididymal sperm.** (**A**) Representative transmission
604 electron microscopy (TEM) images of cauda epididymal sperm mitochondria. (**B**) Statistical
605 analysis of TEM.

606

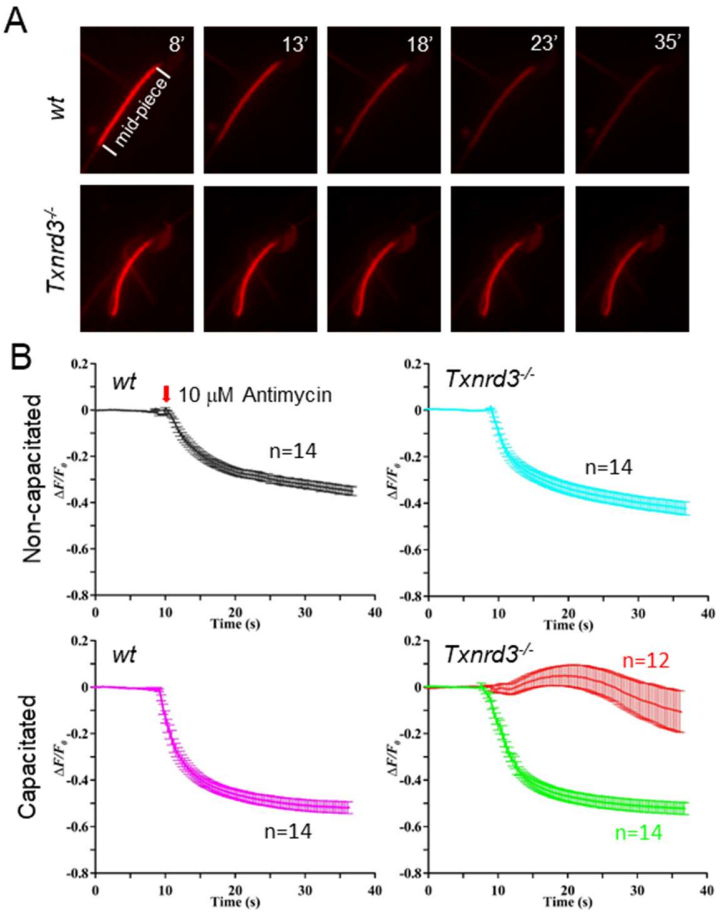

607

608 **Figure 6. Mitochondrial activity, indicated by membrane potential, is impaired in absence of**
609 **TXNRD3.** (**A**) Dynamic representative of mitochondrial membrane potential (**B**) Transition of
610 mitochondrial membrane potential. Capacitated *Txnrd3*$^{-/-}$ sperm show heterogeneous response to
611 antimycin A, an inhibitor of electron transport chain, suggesting disrupted cellular respiration.
612

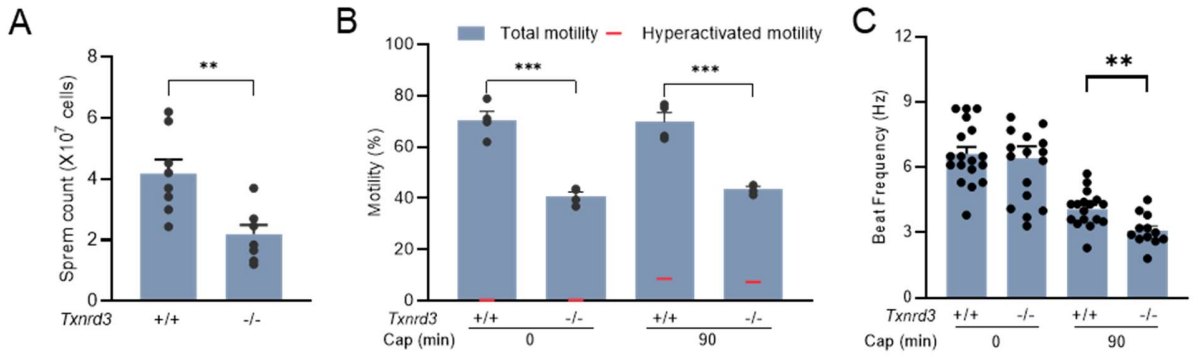

Supplementary Figure 1. TXNRD3-deficient mice exhibit reduced sperm count and motility. (**A**) Epididymal sperm count (Mean ± SEM) from littermates at ages of 3-4 months of age. (**B**) Sperm total motility and hyperactivated motility before and after incubating under capacitation conditions. (**C**) Flagellar beat frequency of *wt* and *Txnrd3*$^{-/-}$ sperm before (0 min, *wt*, 6.6 ± 0.3 Hz; *Txnrd3*$^{-/-}$, 6.4 ± 0.5 Hz) and after (90 min, *wt*, 4.1 ± 0.2 Hz; *Txnrd3*$^{-/-}$, 3.1 ± 0.2 Hz) capacitation. Mean ± SEM, n = X each group. $^{**}p < 0.01$, $^{***}p < 0.001$.

Supplementary Video 1. Head-tethered sperm from *wt* and *Txnrd3*$^{-/-}$ mice before and after incubating under capacitation conditions.

Supplementary Video 2. Free-swimming sperm from *wt* and *Txnrd3*$^{-/-}$ mice before and after incubating under capacitation conditions.

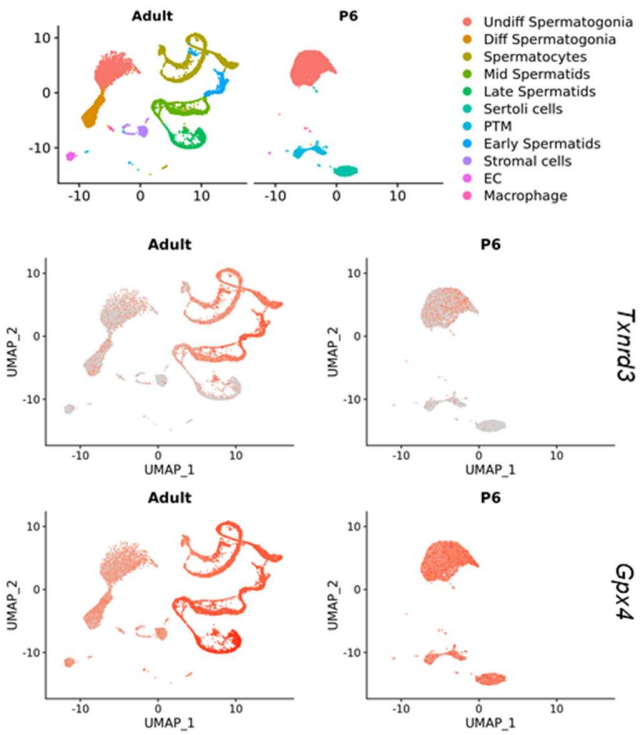

625

626 **Supplementary Figure 2. Single cell RNA sequencing (scRNAseq) of mouse testis.** Txnrd3
627 mRNA express highly in spermatogonia and spermatocytes but much less in spermatids.
628

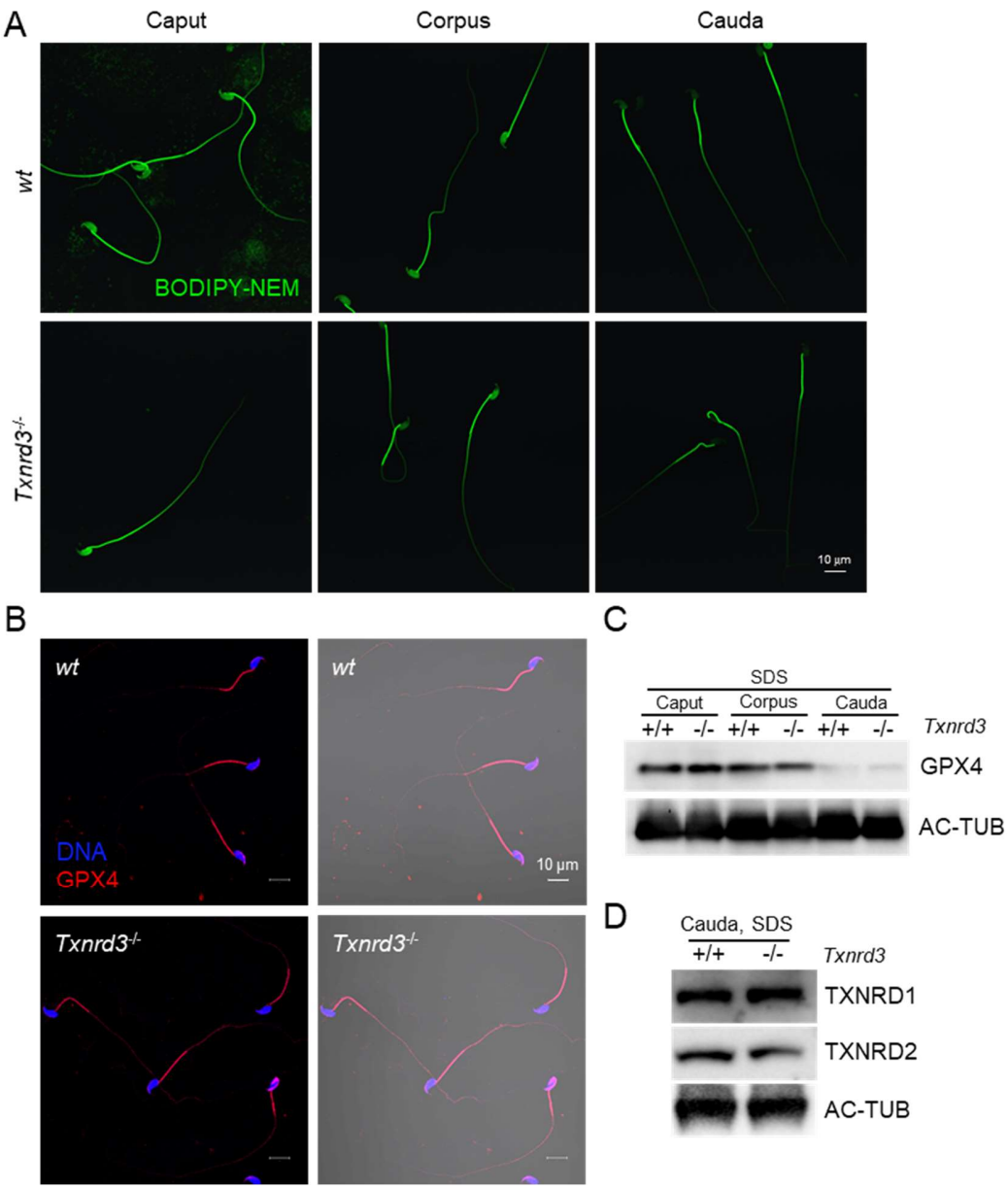

Supplementary Figure 3. Free thiol level and level of GPX4 from caput to cauda sperm. (**A**) Spermatozoa isolated from the caput, corpus and cauda epididymis were incubated with Bodipy-labeled NEM. After quenching with β-mercaptoethanol, free thiol groups in the cells were visualized using confocal microscope. (**B**) Localization of GPx4 (**C**) GPx4 shows descending level in sperm during epididymal transit. (**D**) TXNRD1 and TXNRD2 show same level in both wide type and *Txnrd3*$^{-/-}$ sperm.

637

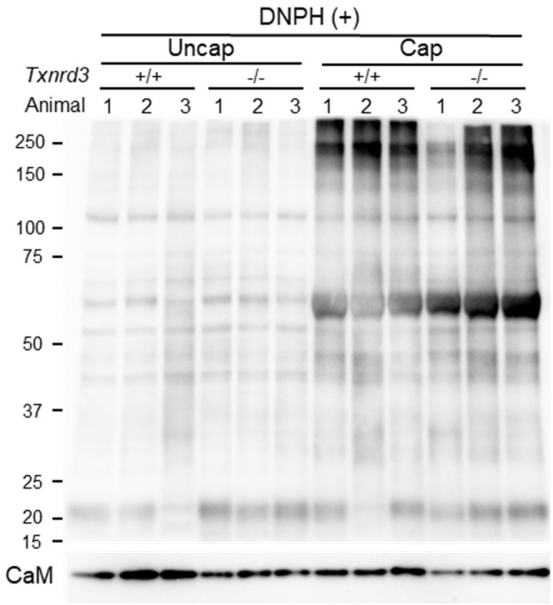

638 **Supplementary Figure 4. Protein oxidation status indicated by protein carbonylation level**
639 **in multiple mice.**

640

641

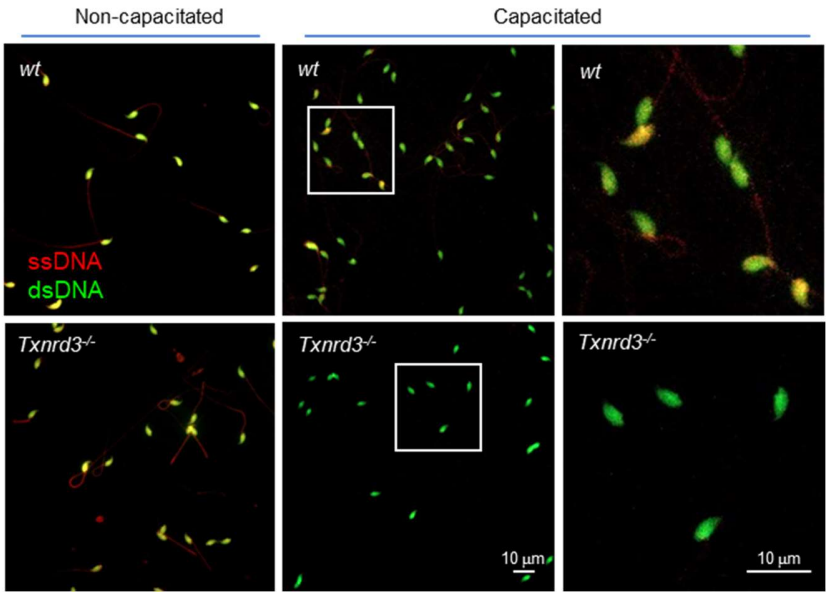

642 **Supplementary Figure 5. Evaluation of DNA state by Acridine Orange assay.** After HCl
643 incubation, *Txnrd3*$^{-/-}$ sperm generated less single-stranded DNA after capacitation, indicating more
644 resistance to acid denaturation. Single-stranded DNA (Red), double-stranded DNA (Green).
645

646

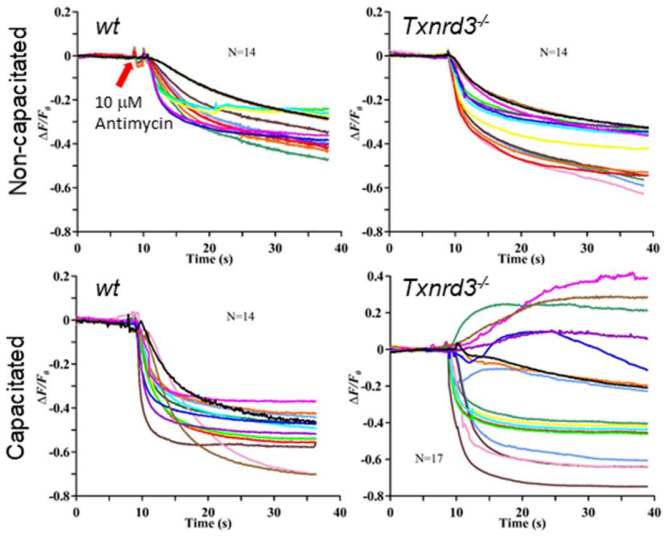

647 **Supplementary Figure 6. Individual traces of mitochondrial membrane potential transition**
648 **from wild type and *Txnrd3*$^{-/-}$ sperm.**

649